

“© 2022 IEEE. Personal use of this material is permitted. Permission from IEEE must be obtained for all other uses, in any current or future media, including reprinting/republishing this material for advertising or promotional purposes, creating new collective works, for resale or redistribution to servers or lists, or reuse of any copyrighted component of this work in other works.”

# Multipole-based Electrically Small Unidirectional Antenna with Exceptionally High Realized Gain

Ting Shi, *Member, IEEE*, Ming-Chun Tang, *Senior Member, IEEE*, Ruolei Chai, *Student Member, IEEE*, and Richard W. Ziolkowski, *Life Fellow, IEEE*

**Abstract**—Electrically small, high-directivity antennas are in demand for a variety of current and future wireless applications. An electrically small directive antenna (ESDA) that requires only one specially-engineered port to excite a set of multipoles is demonstrated in this paper. Four 90° copper sectors are combined with additional structures and fed with a coaxial cable. Two resonant quadrupoles (equivalent to two pairs of resonant electric dipoles) and one magnetic dipole are excited. Both high radiation efficiency and good impedance matching are achieved. Theoretical calculations, numerical simulations, and experimental measurements are shown to be in good agreement. An optimized prototype is designed, fabricated, and tested. The measured results confirm that it is a supergain system. The unidirectional ESDA has a peak directivity of 6.71 dBi, a peak realized gain of 6.31 dBi, a radiation efficiency of 94.5%, and a front-to-back ratio of 14.89 dB at its resonance frequency, 814 MHz. Its height is 0.06  $\lambda_{\text{res}}$  and  $ka = 0.98$ . These measured realized gain and directivity values exceed both the Harrington and Kildal-Best  $ka$ -based upper limits.

**Index Terms**—Electrically small antenna, high realized gain, highly directive pattern, multipole, single port, unidirectional.

## I. INTRODUCTION

ANTENNAS with both compact size and high gain are very attractive for current and future wireless systems. They would occupy only a small portion of the space available in them, and they would require less power to fulfill system performance requirements [1], [2]. As a consequence, they provide value to many engineering applications including, for instance, long-distance and point-to-point wireless communication systems [3], radio frequency identification devices (RFIDs) [4], and wireless sensor systems [5]. Nevertheless, passive electrically small antennas have inherent performance limitations and challenges as a consequence of fundamental

electromagnetic reasons. There has been a myriad of studies attempting to ever more precisely define them [6]–[13]. Initially, Chu [8] and Harrington [9] showed that their maximum directivity is  $D_{\text{max}} = N^2 + 2N$ , where  $N$  represents the upper bound on the spherical modes, i.e., multipoles, that contribute to the far-field radiated power. They also suggested that if  $k$  represents the free-space wavenumber and  $a$  represents the radius of the smallest sphere enclosing the entire antenna system, then a good approximation to the number of multipoles available in the emission physics is  $N = ka$ . Hansen critiqued many of these issues [10] and noted, in particular, that a radiator can be called a superdirective antenna when its directivity exceeds the maximal value  $4\pi A/\lambda^2$  obtained when the antenna’s cross-sectional area  $A$  is uniformly excited [11]. A heuristic formula,  $D_{\text{max}} = (ka)^2 + 3$ , was proposed recently by Kildal, Best, et al., to capture the fundamental directivity limitation from small single-port antennas to antennas of any size [12], [13]. It is important to realize, however, that these “bounds” must be understood in the context of the specific physical constraints imposed in determining them. As noted and shown in [14], [15], it is well known that there is no theoretical limit on the directivity. Simply, for instance, let a lossless antenna system radiate a set of multipoles with their maximum  $N \rightarrow \infty$ . However, as soon as one introduces constraints on any superdirective system, then there is. For example, as nicely shown in [15], different amounts of conductor losses alone enforce different finite limits.

Various types of antennas and arrays with finite size have been reported in the pursuit of an improved realized gain. Uzkov initially demonstrated that the maximum end-fire directivity of a linear array of  $N$  isotropic radiators approaches  $N^2$  when the interelement distance vanishes [16]. Based on this design framework, various antennas, e.g., half-wave dipoles [17], [18], folded dipoles/monopoles [19], [20], meander-line dipoles [21], magnetic dipoles [22], quarter-wave monopoles [23], helical monopoles [2], and metamaterial-inspired monopoles [24], have been used to form dual- or multi-element arrays with close interelement spacing (typically less than a one-quarter wavelength) to achieve superdirective behavior from a system having a compact size. However, note that most of these reported compact high-gain arrays are not electrically small, i.e., their electrical size  $ka > 1$ .

One reason is that many of the example elements themselves are half-wavelength types of dipoles. A second reason is efficiency. As the array spacing becomes small, e.g., less than  $0.1 \lambda_0$ , oppositely direct currents often lead to cancellations of the radiated fields. While the directivity remains high, the

Manuscript received December 2, 2021; revised January 12, 2022; accepted January 18, 2022.

This work was supported in part by the National Natural Science Foundation of China contract number 62101104 and 62031006, in part by the China Postdoctoral Science Foundation under Contract 2020M683283, and in part by the Australian Research Council grant number DP160102219. (*Corresponding author: Ming-Chun Tang*)

T. Shi is with the School of Electronic Science and Engineering (National Exemplary School of Microelectronics), University of Electronic Science and Technology of China, Chengdu, 610054, China and also with the School of Microelectronics and Communication Engineering, Chongqing University Chongqing 400044, China (E-mail: tingshi@uestc.edu.cn).

M.-C. Tang and R. Chai are with the Key Laboratory of Dependable Service Computing in Cyber Physical Society Ministry of Education, School of Microelectronics and Communication Engineering, Chongqing University, Chongqing 400044, China (E-mail: tangmingchun@cqu.edu.cn).

R. W. Ziolkowski is with the University of Technology Sydney, Global Big Data Technologies Centre, Ultimo NSW 2007, Australia (E-mail: Richard.Ziolkowski@uts.edu.au).

overall gain substantially decreases. This effect is further exacerbated with electrically small elements that are generally poor radiators themselves. A third reason is the increasing impact of the mutual coupling between the elements as the interelement distances decrease which makes impedance matching a challenge. These features have limited the development of compact dense arrays exhibiting high gains. This is particularly true of superdirective arrays which are well-known to suffer from these issues. Nevertheless, several interesting systems that used electrically small radiators have been reported. For example, two-element driven and parasitic pairs of resonant top-loaded, folded monopole wire elements were successfully designed and measured in [20]. The endfire directivity of these super-gain arrays reached  $\sim 7$  dBi. However, the prototypes required careful matching of the source(s) to their unusual input impedances. Moreover, they were physical arrays of antennas rather than an integrated single element. The parasitic version was a single-port two-element system whereas the driven array was a two-port two-element one. Furthermore, the peak directivity was emphasized with little regard for the backlobe behavior.

Single-port electrically small antennas (ESAs) have been intensely investigated, particularly because of their importance to a wide variety of wireless applications. Their conventional designs are reviewed in textbooks, e.g., [25]; reviews of the basic physics and engineering of unconventional designs exist, e.g., [26]-[28]; and extensive comparisons of their performance have been made, e.g., [29]. Typically, both standard electrically small electric and magnetic dipole antennas radiate dipolar doughnut-shaped patterns, i.e., figure-eight pattern in the plane containing the dipoles and an omnidirectional pattern in the orthogonal plane. A variety of approaches have been taken to improve the directivity of an ESA. Examples that increased it by approximately 3 dB include the introduction of artificial magnetic conductors [30], electromagnetic bandgap structures [31], [32], and slot-modified [33] ground planes. Others include combinations of electric and magnetic dipoles realized as near-field resonant parasitic (NFRP) elements to achieve endfire [34]-[36] and broadside [37]-[40] radiating Huygens dipole antennas (HDAs). Moreover, their cardioid patterns yield high front-to-back ratio (FTBR) values. Quasi-Yagi ESAs with/without an imaging ground plane arrange similar elements into an array configuration to realize high gain endfire radiated fields [41]-[45].

A specially engineered, multipole-based, broadside-radiating, unidirectional, electrically small directive antenna (ESDA) is developed in this paper whose directivity exceeds both the Harrington and Kildal-Best  $ka$ -based upper limits on the directivity. It is a simple, low-profile, low-cost, single-port system. It is a single radiator; there are no physically separate, additional radiating elements. There is no ground plane involved. Nevertheless, its structure and excitation method facilitate the activation of several multipole modes which naturally act as the combination of a two-element quadrupole array, two electric dipoles, and a magnetic dipole. It is experimentally demonstrated that its simulated high realized gain and unidirectional performance are achieved. Detailed descriptions of its design, operating

principles, simulation parameter studies and prototype's measurement results are presented as follows. The multipole design model (MDM) is first introduced in Section II. The overall design methodology and its operating principles are then presented using several dipole-based models and simple antenna cases. Emphasis is given to explain its directivity, its impedance matching to a  $50 \Omega$  source, and its high radiation efficiency (RE). The realization of the optimized high-directivity ESDA prototype and the measurements of its performance characteristics are described in Section III. It is demonstrated that it is the only single-port single-element antenna to date whose measured realized gain exceeds the maximum directivity calculated with either the Harrington or Kildal-Best  $ka$ -based heuristic formula. Next, how the control of the excitation phase and magnitude is actually achieved is detailed in Section IV. An extensive table and related discussions that compare the characteristics of the developed unidirectional ESDA with other systems reported in the literature are given. Finally, some conclusions are drawn in Section V. The directivity analysis of the ESDA is detailed in an Appendix.

We note that all of the numerical simulations of the reported designs and their optimized configurations were performed using the commercial software ANSYS/Ansoft HFSS [46], version 19. The metallic elements in all of them were chosen to be copper with its known material parameters:  $\epsilon_r = 1.0$ ,  $\mu_r = 0.999991$ , bulk conductivity  $\sigma = 5.8 \times 10^7$  S/m, and thickness of 0.5 mm. All of the analytical expressions were calculated with their corresponding MATLAB [47] routines.

## II. OPERATING PRINCIPLES AND DESIGN METHOD

The MDM is introduced to provide a common platform to discuss the electromagnetics of the ESDA system. An evolutionary path from a bow-tie dipole antenna to the final design is used to help understand its operating principles. The relevant electromagnetic concepts follow from the combinations of several multipoles described in [48] that facilitate, in principle, high directivity systems. They properly described the quadrupole-based antenna developed in [49] and provide a very suitable archetype for the ESDA's development.

### A. Multipole Design Models

The MDM in Fig. 1(a) has two simple engineering exemplars, i.e., the two-port two-element array and a single-port parasitic antenna. One important issue for any closely-spaced two-element arrays is the strong mutual coupling that exists between the dipoles. It causes input impedance mismatch and a reduction in the RE. Another issue for the two-port system is that a phase shift element would be required to achieve the opposite current moments. On the other hand, the single-port exemplar is the well-known quasi-Yagi antenna configuration. It simplifies the matching and decoupling issues. Nevertheless, in the absence of a controlled, powerful excitation of the electrically small parasitic element, it does not produce sufficient scattered field strength to yield a supergain result.

The high-density MDM shown in Fig. 1(b) is the basis of the ESDA design. It consists of two resonant quadrupoles (two

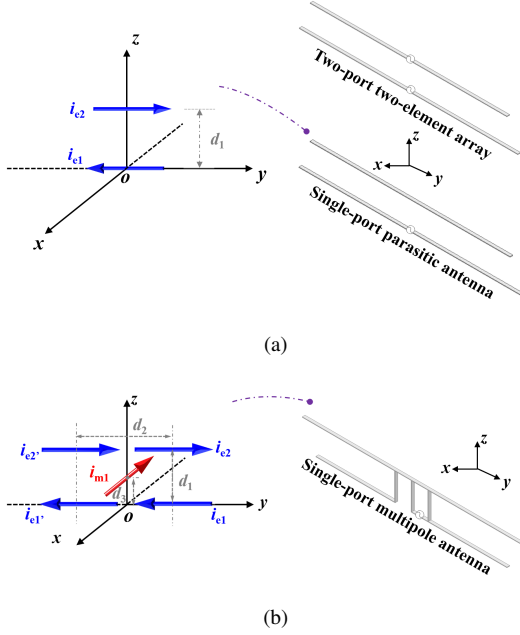


Fig. 1. MDMs of sets of dipole elements and their realizable configurations. (a) Elementary quadrupole system configured as a pair of closely spaced, oppositely oriented electric dipoles. (b) High-density multipole system consisting of a pair of electric quadrupoles and one magnetic dipole.

pairs of resonant electric dipoles) combined with a magnetic dipole. The exemplar is a single-port system that has the multiple dipoles directly connected to and fed by it. The MDM dipoles are labeled by their currents. The dipole element  $i_{e1}$  ( $i_{e2}$ ) is identical to  $i_{e1'}$  ( $i_{e2'}$ ); their center-to-center distance is  $d_2$ . The dipoles  $i_{e1}$  and  $i_{e2}$ , and  $i_{e1'}$  and  $i_{e2'}$  form quadrupole elements. These four dipoles thus form a linear two-element quadrupole array along the y-axis with the element separation distance being  $d_2$ . The magnetic dipole  $i_{m1}$  is taken to be non-resonant and located a distance  $d_3$  along the z-axis. It mainly provides a high inductance required in the actual ESDA for nearly complete impedance matching to a 50- $\Omega$  source.

Referring to the Appendix, the directivity patterns radiated by the MDMs are readily calculated simply as a superposition of the fields radiated by its elemental dipoles. The dipole expressions are taken to be:  $i_{en} = I_{en} l_{en} e^{j\varphi_{en}}$ , where  $n = 1, 1', 2, 2'$ ; and  $i_{m1} = I_{m1} l_{m1} e^{j\varphi_{m1}}$ . The current moment magnitudes (CMMs) are set to be:  $I_{e1} l_{e1} = I_{e1'} l_{e1'}$  and  $I_{e2} l_{e2} = I_{e2'} l_{e2'}$ . They are normalized by that of the electric dipole  $i_{e1}$ , i.e., by  $I_{e1} l_{e1}$ , to simplify the analysis. Similarly, the phase of the current moments of  $i_{e1}$  and  $i_{e1'}$  ( $i_{e2}$  and  $i_{e2'}$ ) is  $\varphi_{e1}$  ( $\varphi_{e2}$ ) and that of  $i_{m1}$  is  $\varphi_{m1}$ . Again to simplify the analysis, these phases are set to be  $\varphi_{e1} = \varphi_{m1} = 0$  and the relative phase difference is denoted  $\varphi = \varphi_{e2} - \varphi_{e1}$ . The distances are those of the final optimized design and fabricated ESDA prototype:  $d_1 = 0.06 \lambda_{res}$ ,  $d_2 = 0.15 \lambda_{res}$  and  $d_3 = 0.03 \lambda_{res}$ .

Two analytical parametric studies were carried out to clarify the relationships between the directive performance and these multiple dipole sources. The corresponding MATLAB calculated directivity and FTBR distributions are shown in Fig. 2. The first study considered how to make the best selection between the optimum directivity and FTBR values as functions

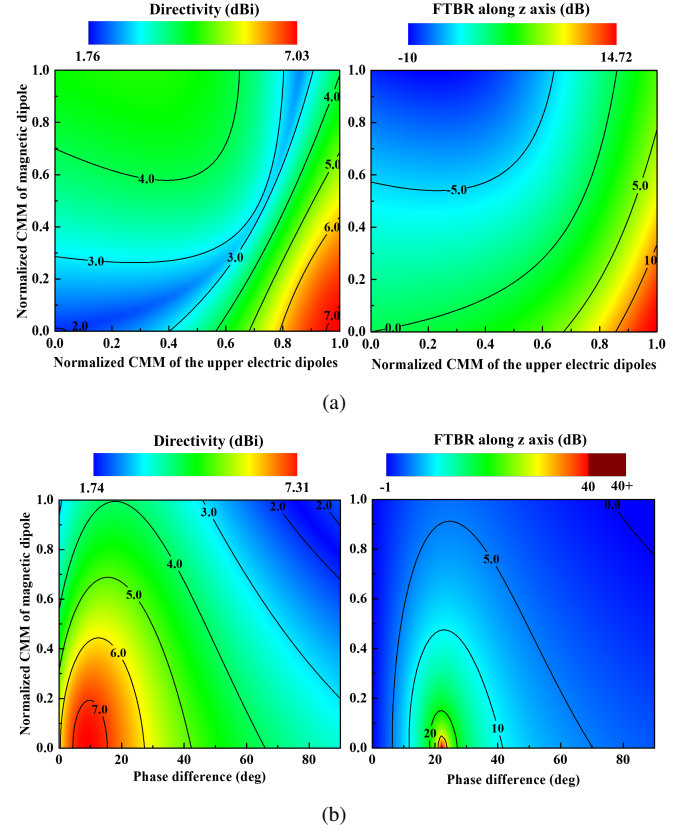


Fig. 2. The directivity and FTBR values of the high-density MDM. (a) As functions of the normalized CMM of the upper electric dipoles and the magnetic dipole. (b) As functions of the phase difference  $\varphi = \varphi_{e2} - \varphi_{e1}$  and the normalized CMM of the magnetic dipole.

of the CMMs of the upper dipoles and the magnetic dipole, i.e., with the normalized CMM values  $I_{e2} l_{e2} = I_{e2'} l_{e2'}$  and  $I_{m1} l_{m1}$  varying, when the phase difference  $\varphi = 14.6^\circ$ . The MATLAB calculated directivity and FTBR distributions are displayed in Fig. 2(a). The maximum values of the directivity, 7.03 dBi, and FTBR, 14.72 dB, were obtained when  $I_{m1} l_{m1} \rightarrow 0$  and  $I_{e2} l_{e2} (I_{e2'} l_{e2'}) \rightarrow I_{e1} l_{e1} (I_{e1'} l_{e1'})$ . Thus, the CMM of the magnetic dipole should be taken to be small since it has only a slight impact on the forward radiation characteristics. Moreover, the CMMs of the upper and lower electric dipoles should be as close as possible. The second study thus set the normalized CMMs of the electric dipoles to be:  $I_{e1} l_{e1} : I_{e1'} l_{e1'} : I_{e2} l_{e2} : I_{e2'} l_{e2'} = 1 : 1 : 1 : 1$ . The directivity and FTBR distributions as functions of both the phase difference  $\varphi$  ranging from  $0^\circ$  to  $90^\circ$  and the normalized CMM of the magnetic dipole,  $I_{m1} l_{m1}$ , ranging from 0 to 1 are shown in Fig. 2(b). These numerical results demonstrate that a maximum directivity (FTBR) of 7.31 dBi (+ $\infty$  dB) is obtained when  $I_{m1} l_{m1} \rightarrow 0$  and  $\varphi \approx 8.73^\circ$  ( $22.32^\circ$ ). As demonstrated further in the Appendix, these results demonstrate the inherent tradeoff that exists between the optimum peak directivity and FTBR values. These analytical results illustrate that good control of the phase difference  $\varphi$  and CMMs is necessary to achieve the desired high directivity with as high as possible FTBR [9], [11], [20], [23], [48].



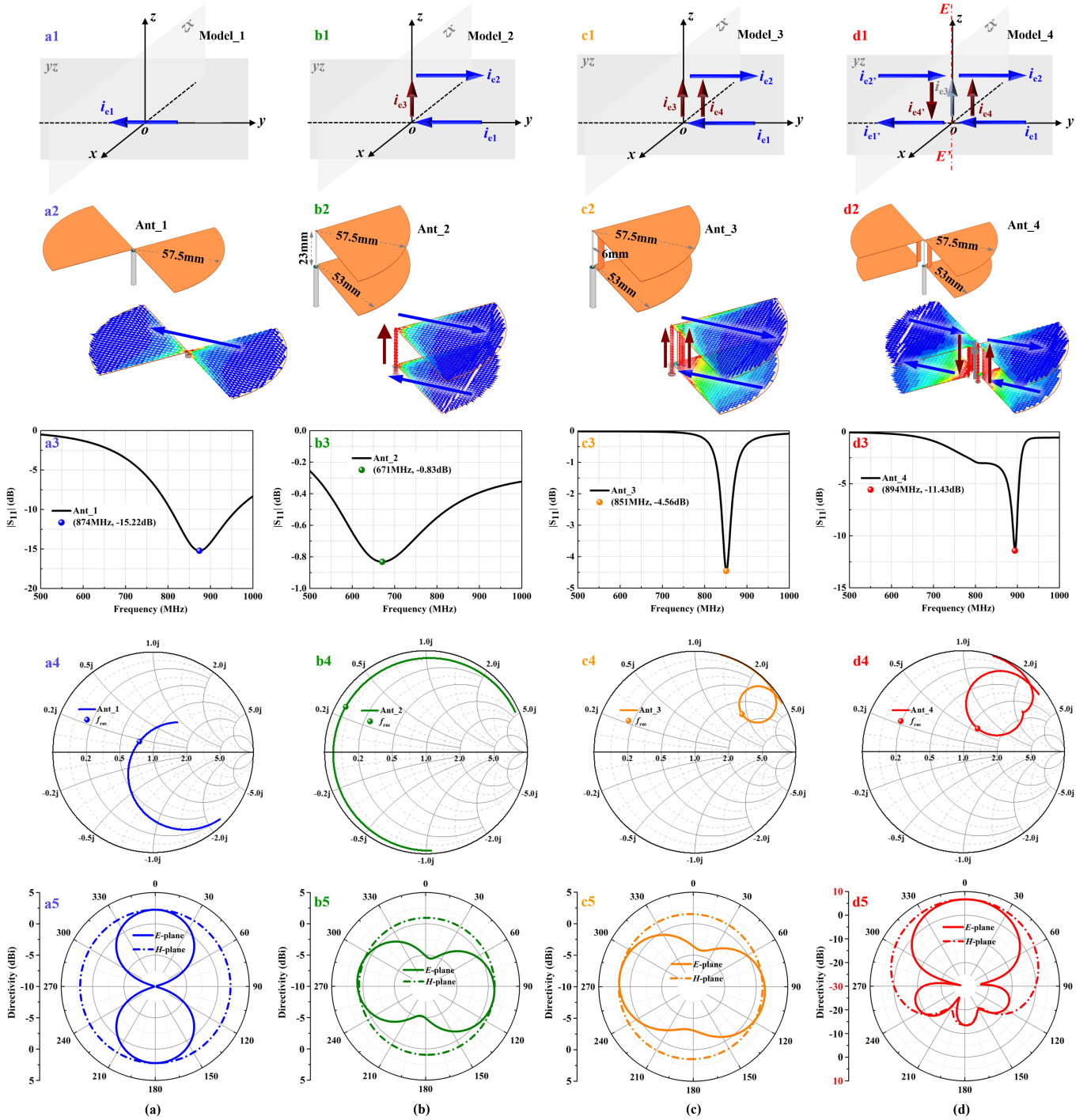


Fig. 3. The ESDA design evolution. Each column presents the MDM; exemplar realization and the surface current density distributions on it;  $|S_{11}|$  values in a rectangular plot and on a Smith chart; and the E- and H-plane directivity patterns at the resonance frequencies indicated in the  $|S_{11}|$  plots. (a) Ant\_1. (b) Ant\_2. (c) Ant\_3. (d) Ant\_4. All of the surface current density subfigures are plotted on the same scale which ranges from 0 (blue) to 20 A/m (red).

### B. Design Evolution

An evolutionary set of four analytical single-port multiple dipole-based models, named Model\_1–Model\_4, and their numerical prototype antennas, Ant\_1–Ant\_4, are used to discuss the operating principles of the ESDA. Each is displayed in Fig. 3 along with their simulated surface current distributions,  $|S_{11}|$  values in both rectangular and Smith chart plots, and the E-

and H-plane directivity patterns at the resonance frequencies indicated in the  $|S_{11}|$  plots.

Column (a) displays Model\_1. It is simply an elemental electric dipole with constant current  $i_{e1}$ . It has a calculated directivity of 1.76 dBi and FTBR = 0 dB. A simple bowtie dipole, Ant\_1, with  $ka = 1.05$  is taken to be its realization. The design follows from the one developed in [50]. The angle of each sector is  $90^\circ$ . Ant\_1 is well impedance matched to the

source with  $|S_{11}|_{\min} = -15.22$  dB, and it resonates at  $f_{\text{res}} = 874$  MHz. The variation of its  $|S_{11}|$  values are displayed on the Smith Chart from 500 MHz to 1 GHz. Because of its compact size, it exhibits a high reactance ranging from capacitive to inductive values. This small bowtie antenna radiates a typical dipole pattern – a figure-eight shape in its E ( $yz$ )-plane and an omnidirectional circle shape in its H ( $zx$ )-plane. Its HFSS simulated directivity is 2.28 dBi, realized gain is 2.17 dBi, and FTBR = 0.01 dB.

Column (b) displays Model\_2. It consists of one pair of oppositely oriented horizontal dipoles with constant currents  $i_{e1}$  and  $i_{e2}$ , and a vertical electric dipole with constant current  $i_{e3}$ . Ant\_2 is then constructed as a pair of bow-tie elements, one above the other. The top one is connected to the center conductor of the coax and the bottom one is connected to its outer wall. This configuration gives the desired opposite current moments on the bow-ties. The presence of the coax segment makes Ant\_2 act as a U-shaped element, which is known to act primarily as a magnetic dipole, but can also have strong electric dipole characteristics depending on how it is excited [51], [52]. The angular extent of the sectors is again  $90^\circ$ . The separation between the sectors is 23 mm, corresponding to approximately  $0.05 \lambda_{\text{res}}$  at the resonance frequency,  $f_{\text{res}} = 671$  MHz. It is a low-profile design. The radius of the top (bottom) sector is 57.5 (53.0) mm or  $0.129 \lambda_{\text{res}}$  ( $0.119 \lambda_{\text{res}}$ ). The impedance match is poor with  $|S_{11}|_{\min} = -0.83$  dB at  $f_{\text{res}}$  because  $Z_{\text{input}} = 2.56 + j13.13 \Omega$ . The simulated directivity is 1.05 dBi, but the realized gain is only -6.78 dBi due to the mismatch. The directivity patterns are clearly a combination of a vertically oriented electric dipole due to the coax extension and the horizontal quadrupole due to the sectors. The vertical dipole and horizontal quadrupole give rise to the omnidirectional character of the H-plane pattern. While the vertical dipole creates a figure-eight pattern in the E-plane, its center is pushed out because of the electric quadrupole's contributions. Moreover, because the phase centers of the dipole and quadrupole are separated along the  $y$ -axis, the quasi-figure-eight pattern is tilted in this plane. This radiator is electrically small at  $f_{\text{res}}$  since  $ka = 0.44$ .

Column (c) displays Model\_3. A second vertical electric dipole element is introduced with constant current  $i_{e4}$ . Ant\_3 is Ant\_2 with a curved vertical strip introduced into it to connect the upper and lower sectors. This strip is centered with respect to the  $y$ -axis at 6.0 mm from the  $z$ -axis, a radius greater than the coax's outer radius. It acts as a shorting pin and provides a shunt inductance. Thus, Ant\_3 appears as a sector version of an inverted-F dipole antenna. The location of the strip was determined initially using IFA design principles. Ant\_3's input impedance thus moves toward the center of the Smith Chart and exhibits a full inductive loop. Its input impedance is now  $Z_{11} = 75.33 + j88.38 \Omega$  at  $f_{\text{res}} = 851$  MHz, which improves its matching level to  $|S_{11}|_{\min} = -4.56$  dB. The directivity pattern in the H-plane remains essentially the same as that of Ant\_2, but the center of the E-plane one becomes a little bit more distorted. The fields radiated by an IFA are known to be a combination of those of an electric and a magnetic dipole. The electric field of its horizontal magnetic dipole reinforces those of the quadrupole. However, the patterns have not changed

much, because the magnetic dipole contribution is weak. The simulated maximum directivity of Ant\_3 at  $f_{\text{res}}$  is 1.81 dBi along the  $z$ -axis, and its realized gain is -0.85 dBi. Thus, Ant\_3 accomplished its purpose – it is a better matched version of Ant\_2.

Column (d) displays Model\_4. A third vertical electric dipole element is introduced whose constant current  $i_{e4'}$  is oriented opposite to that on the coax extension. It is introduced to suppress the power radiated by the coax extension. A second quadrupole is introduced as well. The top (bottom) dipole has the constant current  $i_{e2'}$  ( $i_{e1'}$ ) oriented in the same direction as  $i_{e2}$  ( $i_{e1}$ ). These elements are introduced into Ant\_4 by two sectors centered along the  $-y$ -axis at the same height as those in Ant\_2 and Ant\_3. The top sector is again connected directly to the coax extension. However, the inside end of the bottom sector is displaced from the origin by the same distance, 6.0 mm, as the shorting strip connecting the original two sectors. A second curved vertical strip connects this inside edge of the bottom sector to its top one. The currents on the sectors are in the same direction as those on the original sectors because the current induced on this second strip is opposite to that on the coax's center conductor extension, i.e.,  $i_{e4'} = -i_{e4}$ . Thus, a virtual perfect electric conducting (PEC) wall is produced in the  $zx$ -plane. Because of the asymmetry resulting from the additional structure, this strip current is thus able to convert the undesired radiation mode from the center conductor  $i_{e3}$  into simply a transmission mode [53]. Moreover, the CMMs on the new sectors are essentially identical those on the original ones, i.e.,  $i_{e1} = i_{e1'}$  and  $i_{e2} = i_{e2'}$ . Finally, because of the top sectors are connected to the coax extension, the out-of-phase currents  $i_{e4}$  and  $i_{e4'}$  form a nearly closed U-shaped element that provides a loop mode that yields an equivalent magnetic dipole [54], i.e., the current element  $i_{m1}$  of the MDM in Fig. 1(b).

If the bottom left sector was connected to the outer wall of the coax to remove the asymmetry, the current on the coax extension would dominate the design and it would radiate as a vertically polarized dipole, similar to the widely reported omnidirectional antennas [55]. Because the top and bottom sectors have different radii, the quadrupole is actually incomplete. It is clear from the current density plots that the currents on the top and bottom sectors are slightly different. Determining the current densities at the specified virtual points shows that they have different magnitudes and phases. These differences are introduced by the excitation of the structure and especially the asymmetry in the two halves of the structure. The sectors act as a combination of an electric dipole from each of the top, longer sectors and a quadrupole from the combination of the top and bottom sectors.

The antenna is seen to be reasonably matched without additional efforts with  $|S_{11}|_{\min} = -11.43$  dB at  $f_{\text{res}} = 894$  MHz. Its electrical size is thus  $ka = 1.08$ . The corresponding approximate length of the nearly closed loop forming the magnetic dipole is  $2 \times 23 + 4 \times 6 = 70$  mm =  $0.21 \lambda_{\text{res}}$ . Thus, the magnetic dipole is non-resonant; its inductive contribution helps improve the impedance matching [56]. The peak directivity, 6.77 dBi, and peak realized gain, 6.4 dBi, are along the  $+z$ -axis. The corresponding RE is quite high:

98.85%. Furthermore, the patterns in both the E- and H-planes are basically unidirectional without any ground plane. The FTBR = 20.20 dB. The directivity pattern in the E-plane is narrower than the one in the H-plane because the system is essentially a two-element array in the E-plane. Note that at  $f_{\text{res}}$  the aperture area gives  $4\pi A/\lambda_{\text{res}}^2 = 0.64$  dB. Consequently, Ant\_4 is superdirective by more than an order of magnitude.

The evolution of Ant\_1 to Ant\_4 clearly revealed the major aspects of the ESDA design and how they contribute to its performance. The characteristic parameters of these four designs are summarized in Table I. The design parameters of Ant\_4 were optimized to maximize the realized gain and FTBR values and to achieve an electrically small version in order to define those of the prototype ESDA.

TABLE I  
SUMMARY OF THE SIMULATED RESULTS FOR THE ANTENNAS IN FIG. 3

Examples	Ant_1	Ant_2	Ant_3	Ant_4
$f_{\text{res}}$ (MHz)	874	671	851	894
$ka$	1.05	0.44	0.55	1.08
$ S_{11} _{\text{min}}$ (dB)	-15.22	-0.83	-4.56	-11.43
HFSS Sim. Dir. (dBi)	2.28	1.05	1.81	6.77
Realized Gain (dBi)	2.17	-6.78	-0.85	6.40
FTBR along $z$ -axis (dB)	0.01	0.06	0.36	20.20

### III. ESDA PROTOTYPE AND ITS MEASUREMENTS

A single-port, low-profile, ESDA prototype based on the Ant\_4 concept was designed, fabricated, and measured. The configuration of the optimized ESDA is presented in Fig. 4. Its design parameters are also shown and their optimized values are given in Table II. As shown in Figs. 4(a) and 4(b), the main radiators are four copper 90° sectors. Because the top two are connected, they form a full bow-tie element. The two bottom ones have a radius shorter than the top ones. As shown in Fig. 4(b), a copper arc strip is mounted near the end of each sector. Their presence helps control the phases of the currents on the sectors to attain the desired differences. Because they add capacitance, they aid in reducing the resonance frequency and, hence, the electrical size of the antenna. Fig. 4(b) also indicates that the vertical U-shaped rectangular copper strips connect the sectors; they are attached to them with 2.0 mm diameter screws to ensure good current flow and mechanical stability. Additional design parameter details are provided in Figs. 4(c) and 4(d). The coaxial feed cable has an inner conductor with a 0.94 mm diameter. Its top is connected to the geometric center of the top bowtie, where a 0.94 mm diameter hole is dogged for a precise connection.

The bottom + $y$ -sector is connected directly to the outer wall of the coax. A concentric ring pad is added to this sector to enable its easy soldering to the outer conductor of the coaxial cable. The side view of the ESDA structure is shown in Fig. 4(e). Six virtual points are defined on the surface of the ESDA. The points  $P1_{\text{upper}}$  and  $P1_{\text{lower}}$  are located, respectively, at the centers of the top and bottom of the bottom  $-y$ -sector. The points  $P2_{\text{upper}}$  and  $P2_{\text{lower}}$  are located, respectively, at the center

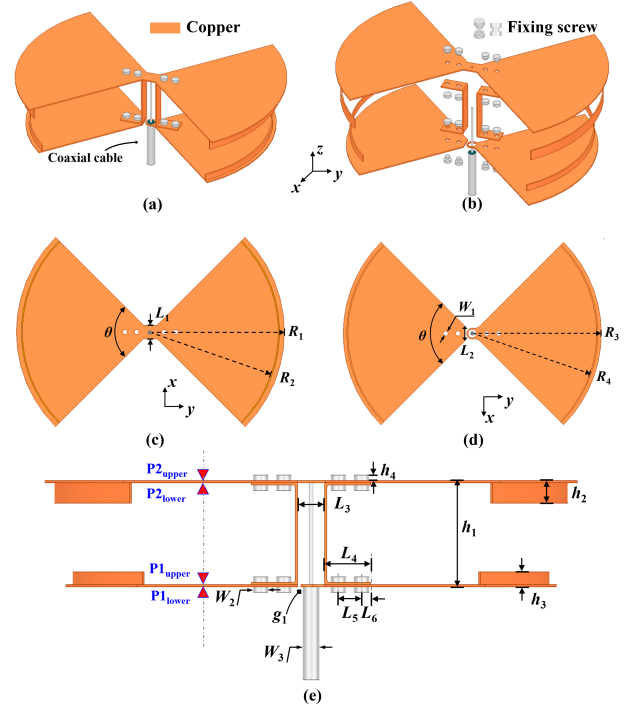


Fig. 4. Configuration of the optimized ESDA. (a) 3-D view. (b) Exploded isometric view. (c) Top view of the lower surface of top bowtie. (d) Top view of the upper surface of bottom two sectors. (e) Side view.

TABLE II  
OPTIMIZED PARAMETERS OF THE ESDA

$R_1 = 57.5\text{mm}$	$R_2 = 54.9\text{mm}$	$R_3 = 53\text{mm}$	$R_4 = 51.1\text{mm}$
$L_1 = 5.94\text{mm}$	$L_2 = 5.8\text{mm}$	$L_3 = 5.8\text{mm}$	$L_4 = 10.0\text{mm}$
$L_5 = 5.00\text{mm}$	$L_6 = 2.0\text{mm}$	$L_7 = 20.0\text{mm}$	$h_1 = 23.0\text{mm}$
$h_2 = 4.9\text{mm}$	$h_3 = 3.2\text{mm}$	$g_1 = 0.63\text{mm}$	$W_1 = 2.0\text{mm}$
$W_2 = 3.2\text{mm}$	$W_3 = 3.31\text{mm}$	$\theta = 90^\circ$	NULL

of the upper and lower surfaces of the top  $-y$ -sector. The points P3 and P4 are located halfway up the U-shaped vertical strip on their outside surfaces. The surface current densities at these six points were extracted from the numerical simulations for discussion in Section IV.

The prototype ESDA was fabricated, assembled, and tested with a sleeve balun attached. Photos of all of its components and the assembled prototype are presented in Figs. 5(a) and 5(b), respectively. Note that the ESDA is a balanced dipole-based system, whereas the coax feed is unbalanced. Hence, a 87 mm long sleeve balun was employed to make the transition between unbalanced and balanced components to prevent the coax from radiating power or picking up any noise [57]. The  $S$ -parameters were measured using an Agilent E8361A PNA vector network analyzer. The antenna measurement system from MVG with a model number STARLAB 18 GHz was used at the National Key Laboratory of Science and Technology of China. The ESDA under test in it is shown in Fig. 5(c) with the balun attached.

The measured and simulated performance characteristics of

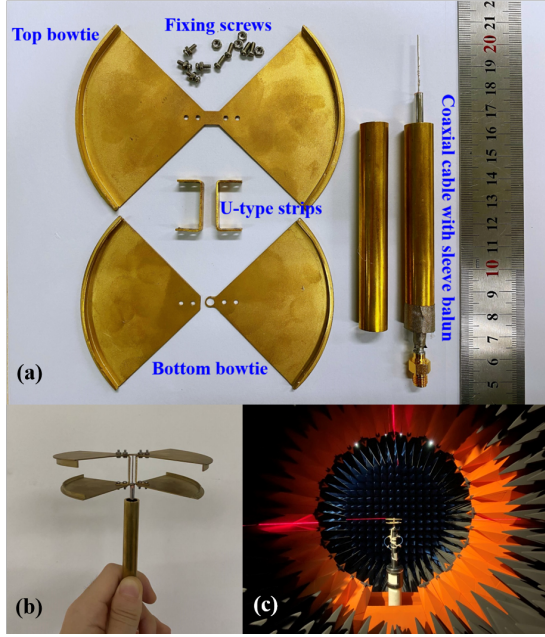


Fig. 5. Photographs of the ESDA prototype and its experiment setup. (a) Views of each component before assembly and the sleeve baluns. (b) Side view of the assembled ESDA mounted on a sleeve balun. (c) 3-D isometric view of the ESDA under test in the anechoic measurement chamber.

the prototype ESDA are presented in Fig. 6. Fig. 6(a) indicates that good impedance matching was achieved with the balun being present. The measured (simulated)  $-10$ -dB impedance bandwidth ranges from 808.5 to 818.2 MHz (810.77 to 821.28 MHz), yielding a fractional bandwidth (FBW) of 1.2% (1.3%). The measured (simulated) resonance frequency is 814 (816) MHz with  $|S_{11}|_{\min} = -14.6$  ( $-15.4$  dB). Corresponding to the wavelength at  $f_{\text{res}} = 814$  MHz, the electrical size  $ka = 0.98$  (0.98); the height,  $0.06 \lambda_{\text{res}}$ , is low profile; and the area of the circle encompassing the top bow-tie element is  $A_{\text{ESDA}} = \pi \times 0.152^2 \lambda_{\text{res}}^2 = 0.07 \lambda_{\text{res}}^2$ .

The measured and simulated E- and H-plane realized gain patterns of the ESDA with the balun attached are compared in Fig. 6(b). The measured (simulated) peak realized gain value is 6.31 (6.62) dBi at  $f_{\text{res}} = 814$  (816) MHz in the broadside direction (+z-axis) with the FTBR = 14.89 (12.18) dB and the RE = 94.5% (98.17%). The 1-dB gain and realized gain bandwidths were from 803.6 to 837.2 MHz (4.1% FBW) and 808.8 to 825.5 MHz (2.0% FBW), respectively, indicating a rather flat realized gain profile over the impedance bandwidth centered at  $f_{\text{res}}$ . The corresponding measured (simulated) directivity is 6.71 dBi (6.75 dBi). The measured (simulated) half-power beamwidths were  $71.42^\circ$  ( $70.34^\circ$ ), ranging from  $-34.27^\circ$  to  $37.15^\circ$  ( $-34.49^\circ$  to  $35.85^\circ$ ) in the E-plane, and  $113.44^\circ$  ( $119.84^\circ$ ), ranging from  $-54.32^\circ$  to  $59.12^\circ$  ( $-59.95^\circ$  to  $59.89^\circ$ ) in the H-plane, respectively. Notice that the simulated and measured cross-polarization levels are very small. Also notice that the half-power beamwidth in the E-plane is significantly narrower than in the H-plane because it contains the two-element quadrupole array. Moreover, there is a subtle asymmetry observed in the simulated and measured E-plane patterns due to the asymmetrical configuration of the bottom

two sectors. The simulated 3-D directivity pattern at the simulated  $f_{\text{res}} = 816$  MHz is presented in Fig. 6(c).

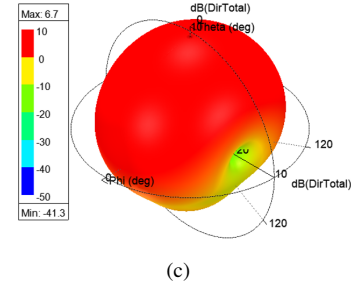
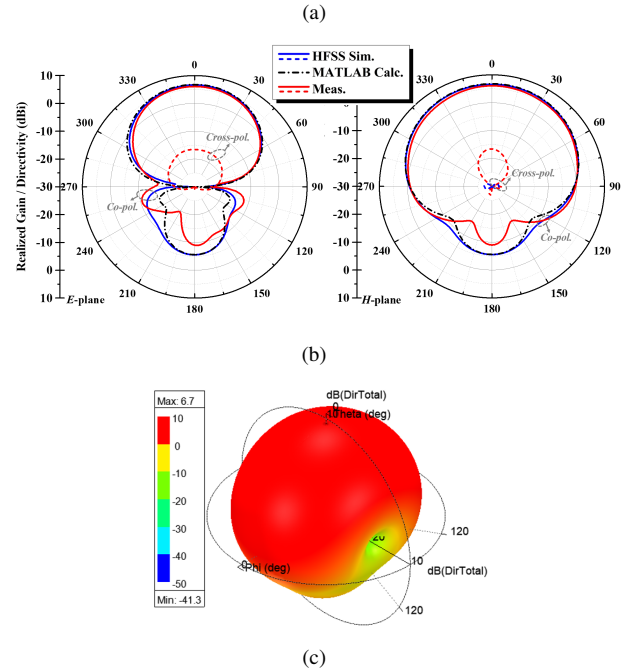
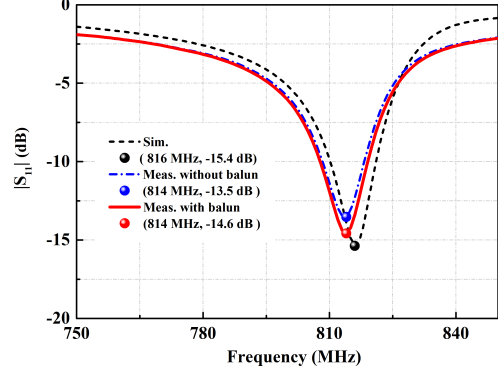


Fig. 6. Simulated and measured results of the ESDA prototype. (a)  $|S_{11}|$  values. (b) Analytical, HFSS simulated and measured realized gain and directivity patterns in the E- and H-planes at their respective resonance frequency. (c) Simulated 3-D directivity pattern at 816 MHz.

In order to demonstrate that the analytical MDM model reproduces these simulation results, its CMMs and phase difference values were obtained, as explained in the Appendix, by curve fitting the predicted directivity patterns to those obtained from the HFSS simulations. These values are, respectively,  $I_{e1'l_{e1}} : I_{e1'l_{e1'}} : I_{e2'l_{e2}} : I_{e2'l_{e2'}} : I_{m1'l_{m1}} = 1.0 : 1.0 : 0.92 : 0.92 : 0.02$  and  $\varphi = 14.6^\circ$ . The MDM terms were also obtained in a different manner from the simulated average current amplitudes at the six virtual points. This approach is discussed in more detail in the next section in relation to Table III. They are  $I_{e1'l_{e1}} : I_{e1'l_{e1'}} : I_{e2'l_{e2}} : I_{e2'l_{e2'}} : I_{m1'l_{m1}} = 1.0 : 1.0 : 0.88 : 0.88 : 0.02$ , and  $\varphi = 10.45^\circ$ . Both sets of MDM values agree reasonably well.

With the ESDA prototype's distances:  $d_1 = 0.06 \lambda_{\text{res}}$ ,  $d_2 = 0.15 \lambda_{\text{res}}$ ,  $d_3 = 0.03 \lambda_{\text{res}}$ , the MDM's MATLAB cal-



culated directivity patterns using the curve-fit MDM terms are included in Fig. 6 for comparison. The peak directivity is 6.78 dBi with the FTBR = 12.37 dB. The calculated half-power beamwidths were  $73^\circ$ , ranging from  $-36.5^\circ$  to  $36.5^\circ$  in the E-plane, and  $120.4^\circ$ , ranging from  $-60.2^\circ$  to  $60.2^\circ$  in the H-plane, respectively. Because of the prototype's high RE and good impedance matching, the analytical ESDA model's calculated directivity patterns are quite consistent with the HFSS simulated realized gain patterns.

Overall, the simulated, measured, and calculated results are in good agreement. Nevertheless, note that the measured FTBR is about 2.7 dB higher than the simulated value. The main reason for this difference is that the fabrication and assembly process unavoidably introduced slight errors that led to the phase difference being dissimilar from the simulated value and, hence, to the unexpected increased FTBR. Furthermore, the difference of the measured peak directivity from the simulated value arises from the same issues. The measured peak directivity 6.31 dBi (4.28) is  $4.86 \times (4\pi A_{\text{ESDA}}/\lambda_{\text{res}}^2 = 0.88)$ , which confirms that the ESDA prototype is a super gain system. Moreover, both the peak simulated and measured directivity values of the ESDA exceed the maximum directivity specified by both Harrington's limit and Kildal-Best's heuristic formula limit, i.e., 4.65 dBi and 5.98 dBi, respectively, for  $ka = 0.98$ .

#### IV. ESDA DISCUSSION AND COMPARISONS

The realization of an ESA with super high gain, as noted, is challenging and the peak value is theoretically limited as discussed in [18]. Five reasons were given. They are: 1) the requirement of tight tolerances on the excitation magnitude and phase, 2) impedance mismatch caused by high input reactance and low radiation resistance, 3) low RE caused by increased ohmic losses causing the radiation resistance to be reduced, 4) unsuitable single-port array designs, and 5) narrow bandwidths. Note that Case\_4 in Section II overcame the first four of these by activating multiple dipole modes. The analytical MDM does not facilitate any considerations of the impedance bandwidth. Despite this analytical success, the actual realization of an electrically small system was a more difficult practical challenge. While the ESDA prototype realized good impedance matching and maintained the anticipated peak directivity, the FTBR value was sacrificed. The tradeoff between the directivity and FTBR was illustrated in Fig. 2. The fine tailoring of the excitation amplitudes of the multipoles, i.e., their magnitudes and phase differences, is detailed with numerical support in this section. The salient features of the supergain ESDA prototype are further highlighted with comparisons with systems reported in the literature.

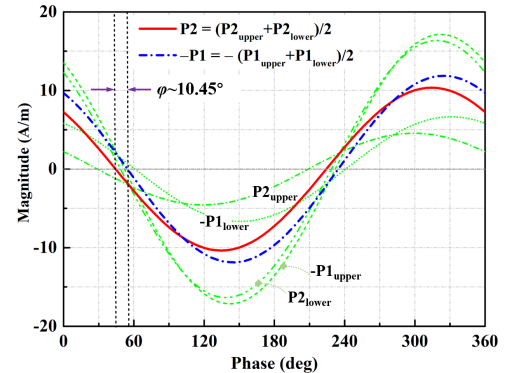
##### A. Analysis of Multipole Amplitude Control

The two U-shaped strips in the ESDA prototype connect its copper sector pairs. A fully connected topology would ensure that the excitation magnitudes of the consequent two bowtie elements would be as close as possible to each other. The asymmetry introduced by the lower sectors being disconnected leads to different current amplitudes. The length ratio of

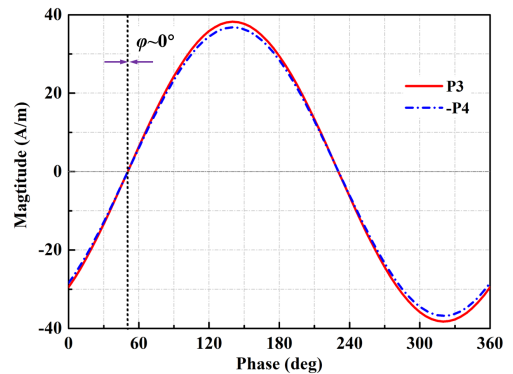
the top bowtie and bottom sectors is directly related to the difference in the phases of the currents on them. The additional arc-shaped strips help finely tailor this phase difference.

To numerically study the excitation magnitudes and their phases, the fields calculator in HFSS was employed to determine the component vector surface current densities at the specified six virtual points, i.e.,  $P1_{\text{upper}}$ ,  $P1_{\text{lower}}$ ,  $P2_{\text{upper}}$ ,  $P2_{\text{lower}}$ , P3 and P4 introduced in Fig. 4. Since the copper thickness cannot be neglected, the surface currents on the upper and lower surfaces of each bow-tie are not identical. The values of the y-component of the surface currents at  $P1_{\text{upper}}$  and  $P1_{\text{lower}}$  ( $P2_{\text{upper}}$  and  $P2_{\text{lower}}$ ) were calculated and their average value is herein associated with the "average" point P1 (P2). These calculated values that are associated with the surface currents on the ESDA simulation model were then used to specify the equivalent CMMs and the phase difference of the electric and magnetic dipoles in the analytical model.

The calculated y-components of the vector surface currents at P1, P2, P3, and P4 are shown in Fig. 7. Recall that the orientations of the  $i_{e1}$  ( $i_{e1'}$ ) and  $i_{e2}$  ( $i_{e2'}$ ) elements were assumed to be opposite. The phase difference  $\varphi$  is taken without involving that initial  $180^\circ$  phase difference.



(a)



(b)

Fig. 7. The current magnitudes at the specified virtual points obtained with the HFSS fields calculator. (a) P1 (average value of  $P1_{\text{upper}}$  and  $P1_{\text{lower}}$ ) and P2 (average value of  $P2_{\text{lower}}$  and  $P2_{\text{upper}}$ ). (b) P3 and P4.

As shown in Fig. 7(a), the phase difference between the two

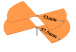



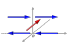
points P1 and P2 is approximately  $\varphi = 10.45^\circ$ . The magnitude ratio at the two points P1 and P2 is approximately 1.0 : 0.88. As shown in Fig. 7(b), there is no phase difference between P3 and P4, and the magnitude of the z-component of the surface currents at these two points is approximately equal. The equivalent dipole result is indeed then the magnetic dipole. These are the values noted in relation to the discussion of Fig. 6.

To further explore the validity of the MDM, the length ratio between the top and bottom sectors in the HFSS numerical model was varied and the results compared with those obtained from it with its curve-fit terms. Four ESA cases were investigated. Their radiated field characteristics were obtained along with their average surface current values at P1 and P2. These simulated results are summarized in Table. III. Case\_1 is the ESDA in Fig. 3 without the four vertical arcs and the two vertical U-type strips. Thus, Case\_1 is basically a sector-based Yagi antenna. The poor impedance match results from the absence of the curved strips and the closer spacing of the sectors – approximately  $0.059 \lambda_{\text{res}}$  at  $f_{\text{res}} = 803$  MHz. Case\_2 is defined by the ESDA without the four vertical arcs and with  $R_1 = 57.5$  mm and  $R_3 = 57.5$  mm. Case\_3 is defined by the ESDA without four vertical arcs and with  $R_1 = 57.5$  mm and  $R_3 = 56.5$  mm. Case\_4 is the final optimized ESDA. Case\_3 has the same small electrical size as Case\_4, but its length ratio between the upper bow-tie and bottom bow-tie is not optimal. By introducing the four vertical arcs present in the prototype into Case\_3, the magnitudes at P1 and P2 are closer to each other and their phase difference,  $10.45^\circ$ , is quite close to the curve-fit value,  $14.6^\circ$ . The improvements in the impedance match, directivity, realized gain, and FTBR values as the cases evolve into Case\_4 are immediately apparent. Moreover, the close agreement of the MDM's radiated field characteristics with the HFSS predicted values is quite clear. Finally, the data in Table III demonstrates that the control of the magnitudes and phases of the currents on the surfaces of the ESDA and its derivatives has a significant impact on their radiation performance.

### B. Comparisons

Performance comparisons of the ESDA prototype with recently reported compact high gain arrays and antennas are provided in Table IV. There is a wide range of characteristics provided including the electrical size, directivity, realized gain, and topology of the structure. Note that many of the references did not directly provide all of the data required in Table IV. Some provided only simulated values. Some parameters were estimated from the available results, e.g., the value of  $ka$  in [18], [19], [21], and [22] was estimated on the basis of their physical sizes; the directivity in [32], [35]-[40] was roughly estimated based on their maximum realized gain and RE values. The rest of the unavailable data is set to be null. We note that the profile parameter is defined as the total distance along the radiation direction for the multi-element arrays [18]-[20], [24] and the parasitic antennas with endfire radiation performance [21], [22], [34]-[36], [41]-[44]. It is the total height of the antennas with broadside radiation performance, e.g., the Huygens [37]-[40] and metal-backed [32-33] ESAs.

TABLE III  
COMPARISON BETWEEN THE SIMULATED RESULTS FOR THE FOUR ANTENNA CASES AND THE CURVE-FIT MDM VERSION

Diff. cases (dBi)	Case_1	Case_2	Case_3	Case_4	MDM
Category					
$f_{\text{res}}$ (MHz)	805	796	815	816	\
$ka$	0.97	1.00	0.99	0.98	\
$ S_{11} _{\text{min}}$ (dB)	-2.89	-7.28	-9.90	-15.4	\
Dir. (dBi)	4.63	4.48	5.10	6.75	6.78
Real. Gain (dBi)	1.52	3.62	4.54	6.62	\
FTBR (dB)	5.62	5.83	8.25	12.18	12.37
Mag. Ratio P1:P2	1 : 0.68	1 : 0.47	1 : 0.76	1 : 0.88	1 : 0.92
Phase diff. at P2 to P1(deg)	21.4	26.36	22.63	10.45	14.60

The  $ka$  calculation for [20] and [22] does not include the total size of the ground plane. Since an electrically large metallic ground plane was utilized to convert their multiple dipole systems into monopole-based ones for the sake of fabrication and measurement, their gain values were calculated with a 3 dB subtraction. The metallic ground planes in [24], [28], [29], and [38] are sufficiently small to be included in the  $ka < 1$  region. The measured gain of these antennas was included without any amendments.

As noted in the Introduction, Harrington provided a maximum directivity bound based on the electrical size  $ka$ . The Kildal-Best heuristic formula does as well for single-port small antennas and single- and multi-port antennas that are large in size. The realized gain parameter is of most importance in practical engineering applications since it accounts for the total efficiency of an antenna in addition to its directivity. Fig. 8 displays the maximum realized gain for the fair comparison cases listed in the table as functions of their  $ka$  values. The curves corresponding to the Harrington and Kildal-Best bounds are also included. The measured realized gain of the ESDA exceeds both of those bounds for  $ka = 0.98$ .

Table IV indicates that the ESDA prototype has one of the lowest profiles and electrical size, and one of the largest FTBR, directivity, RE and realized gain values. Note, however, that several cases from Table IV are excluded in Fig. 8 even though they too surpass the Kildal-Best limit. For example, Ref [18] realized a super high directivity of 12.5 dBi, significantly higher than the Kildal-Best calculated value of 7.9 dBi. However, the authors employed a lossy impedance matching network that significantly degraded the total efficiency leading to a realized gain of less than  $-10$  dBi. On the other hand, data points representing the driven and parasitic systems reported in [20] are included in Fig. 8 for comparison purposes, as they were in Fig. 3 of [13], even though they are two-element monopole arrays with large ground planes. In contrast to the broadside radiating ESDA, their endfire supergain performance

TABLE IV  
COMPARISON OF THE ESDA PROTOTYPE WITH OTHER SUPERGAIN ANTENNAS AND ARRAYS

Refs.	$ka$	FBW (%)	Cross section ( $\lambda_0^2$ )	Profile ( $\lambda_0$ )	Directivity (dBi)	Real. Gain (dBi)	RE (%)	FTBR (dB)	High gain production	With/without ground
[18]	1.79	—	0.45×0.36	0.36	12.5	−18	—	~ 13	Four-element Yagi	No
[19]	1.51	1.9	0.48×0.053	0.053	7.44	7.14	93.4	5.98	Three-element Yagi	No
#[20]	0.7	—	~ 0.14×0.32	~ 0.14	7.0	6.7	—	—	Two-element Array	Yes(−3dB)
	~ 1.0	8.0	—	~ 0.15	7.3	7.0	98.5	—	Two-element Yagi	Yes(−3dB)
*#[21]	0.98	1.2	—	~ 0.145	7.47	—	—	7.48	Three-element Yagi	No
#[22]	1.49	—	—	~0.28	9.2	7.0	61.0	—	Two-element Yagi	Yes(−3dB)
[24]	—	1.4	—	0.1	7.6	1.4	24.0	—	Two-element Array	Yes
[32]	0.99	—	—	0.042	~ 5.33	4.36	~ 80	4.88	AMC-ground ESA	Yes
*[33]	0.94	0.67	~ $\pi \times 0.15^2$	0.1	6.32	5.7	86.87	23.16	Slot-ground ESA	Yes
*#[34]	0.484	1.7	~ $\pi \times 0.07^2$	0.15	4.21	3.47	84.27	23.2	Huygens ESA	No
[35]	0.92	2.73	~ $\pi \times 0.15^2$	0.29	~4.26	3.55	84.9	17.5	Huygens Yagi ESA	No
[36]	0.98	1.32	~ $\pi \times 0.15^2$	0.158	~ 6.11	5.4	85.0	13.3	Huygens Yagi ESA	No
[37]	0.645	0.62	~ $\pi \times 0.1^2$	0.05	~ 4.7	2.03	71.6	16.92	Huygens ESA	No
#[38]	0.961	2.14	~ 0.19 × 0.22	0.106	~ 5.21	~ 4.5	81.14	~ 14	Huygens ESA	No
[39]	0.73	0.83	~ $\pi \times 0.12^2$	0.04	~ 4.37	2.7	68	17.7	Huygens ESA	No
[40]	0.904	0.46	~ $\pi \times 0.14^2$	0.048	~ 3.28	2.15	61.3	12.1	Huygens ESA	No
[41]	0.75	0.5	0.166 × 0.166	0.02	—	3.5	—	4.3	Two-element Yagi	No
[42]	0.7	3.2	~ 0.14 × 0.32	~ 0.1	4.22	3.08	77.0	11.0	Two-element Yagi	No
[43]	0.84	0.34	0.263 × 0.263	0.03	~ 5.44	5.0	90.3	5.4	Two-element Yagi	No
[44]	0.97	2.06	~ 0.27 × 0.22	0.22	5.26	3.57	44.5	13.44	NFRP Yagi ESA	Yes
This work	0.98	1.3	$\pi \times 0.15^2$	0.06	6.71	6.31	94.5	14.89	Multipole ESA	No

\* Only simulated results were provided.

# Several cases were reported, but only the details of one or two of the best performing cases were provided.

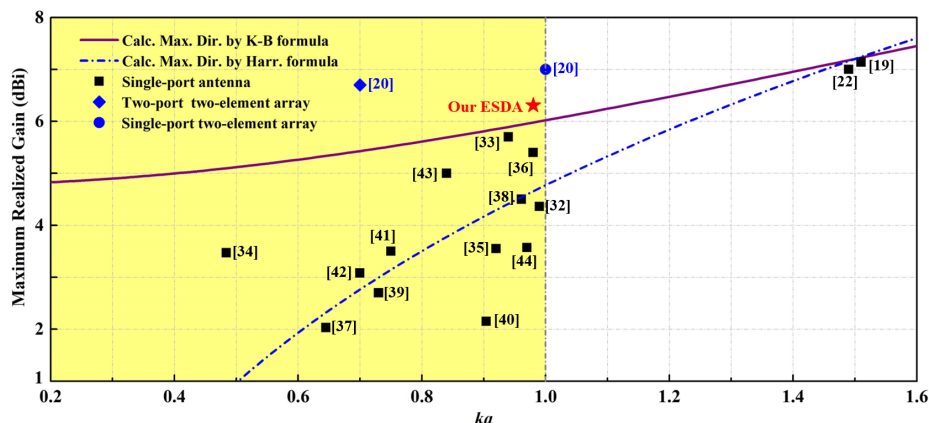


Fig. 8. Comparison of several of the simulated or measured peak realized gain values of the recently reported single-port antennas listed in Table IV to the maximum directivity calculated with the Kildal-Best heuristic and the Harrington formulas as functions of the electrical size  $ka$ .

is achieved because they are arrays.

## V. CONCLUSION

The theoretical analyses, numerical simulations, and experimental measurements of the developed unidirectional ESDA were presented. It was demonstrated that it is a supergain antenna, its peak realized gain exceeding both the Harrington and Kildal-Best upper bounds. It was shown that its superdirective field properties arise from a single-port exciting a

combination of multipoles, i.e., electric and magnetic dipoles and electric quadrupoles. The design overcame the detrimental issues usually associated with a dense system of dipoles including large impedance mismatch, strong mutual coupling, low RE, and difficult control of both the magnitude and phase of the currents excited on the structure. An ESDA prototype was fabricated and measured. The measured results, in good agreement with their simulated and calculated values, exhibited super directivity and realized gain, high RE, and

a good FTBR: 6.71 dBi and 6.31 dBi, 94.5%, and 14.89 dB, respectively. The design is straightforward and easily fabricated. It does not rely on an impedance matching network and does not need mutual coupling suppression, making it a very good candidate for wireless systems that demand compact, low-profile, high efficiency, high directivity antennas. Given the simplicity of its design, the resonance frequency of the developed ESDA can be readily tailored to other frequencies of interest. While an angular sector based dipole and only copper were employed, other dipole or monopole forms combined with high index materials may lead to other multipole-based designs with greater compactness that provide multiple functions, e.g., polarization and multiband versatility.

The bandwidth of the developed ESDA is narrow. Thus, it is currently being considered as a candidate for wireless power transfer (WPT), GPS, RFID and other wireless devices associated with “smart” applications in IoT-related ecosystems. Nevertheless, further efforts are also being considered to expand its bandwidth by, e.g., introducing multiple resonances, employing non-Foster (active) circuits strategies, and/or augmenting it with custom-designed metasurface coverings. Introducing tunable lumped components into the structure to vary its reactance profile could lead to frequency agile versions. Altering the design to efficiently activate additional higher order multipoles [48] and/or developing dense arrays of supergain ESDAs may lead to very desirable systems with yet much higher directivities. The original design could be augmented with an orthogonal version to achieve dual-band and circular polarization performance, as well as dual functionality, e.g., WPT and communication functions. Thus, expectations for a broad range of multipole-based, multifunctional designs based on the ESDA concepts developed herein are indeed high because these types of extensions have been achieved with related Huygens dipole antenna systems [28]. These superdirective multipole-based electrically small antennas would have many attractive features for current 5G and the NextG radiating and receiving systems and their applications.

#### APPENDIX A DIRECTIVITY OF A MULTIPOLE ARRAY

Consider continuous-wave electric and magnetic elemental current densities  $\vec{J}$  and  $\vec{K}$  excited with the angular frequency  $\omega = 2\pi f$  with the selected directions of  $\hat{u}$  and  $\hat{v}$ , respectively, and located at an arbitrary point  $\vec{r}_0 = x_0 \hat{x} + y_0 \hat{y} + z_0 \hat{z}$ :

$$\vec{J} = I_e \ell_e \delta(x - x_0) \delta(y - y_0) \delta(z - z_0) \hat{u} \quad (1)$$

$$\vec{K} = I_m \ell_m \delta(x - x_0) \delta(y - y_0) \delta(z - z_0) \hat{v}$$

The terms  $I_e \ell_e$  and  $I_m \ell_m$  represent, respectively, their electric and magnetic current moments with units  $A - m$ . The electric fields radiated by them into the far-field referenced to the coordinate origin are [46]:

$$\vec{E}_{\omega,J}^{\text{ff}}(\vec{r}) = +j\omega\mu I_e \ell_e G(r) e^{+jk\hat{r}\cdot\vec{r}_0} [\hat{r} \times \hat{r} \times \hat{u}] \quad (2)$$

$$\vec{E}_{\omega,K}^{\text{ff}}(\vec{r}) = +j\omega\mu \left( \frac{I_m \ell_m}{\eta} \right) G(r) e^{+jk\hat{r}\cdot\vec{r}_0} [\hat{r} \times \hat{v}]$$

where  $\mu$ ,  $k$ , and  $\eta$  are the free-space permeability, wave number and wave impedance, respectively. The Greens function of the free-space Helmholtz equation is

$$G(r) = \frac{e^{-jk r}}{4\pi r} \quad (3)$$

The total far-field electric field of an array of  $N$  of these electric dipole and  $Q$  of these magnetic dipole elements follows from basic antenna array theory:

$$\vec{E}_{\omega,J,\text{total}}^{\text{ff}}(\vec{r}) = +j\omega\mu G(r) \sum_{n=1}^N I_{en} l_{en} (\hat{r} \times \hat{r} \times \hat{u}_{en}) e^{+jk\hat{r}\cdot\vec{r}_{en}} \quad (4)$$

$$\vec{E}_{\omega,K,\text{total}}^{\text{ff}}(\vec{r}) = +j\omega\mu \frac{G(r)}{\eta} \sum_{q=1}^Q I_{mq} l_{mq} (\hat{r} \times \hat{v}_{mq}) e^{+jk\hat{r}\cdot\vec{r}_{mq}}$$

For a system formed with  $N$  electric dipoles and  $Q$  magnetic dipoles, the total electric field radiated into their far field can be calculated on the basis of (4) and (5) as follows:

$$\vec{E}_{J,K,\text{total}}^{\text{ff}}(\vec{r}) = \vec{E}_{\omega,J,\text{total}}^{\text{ff}}(\vec{r}) + \vec{E}_{\omega,K,\text{total}}^{\text{ff}}(\vec{r}) \quad (5)$$

Because their fields are transverse electromagnetic in their far field, the Poynting vector of the combined electric and magnetic dipole systems is calculated as:

$$\vec{S}_{\omega,\text{total}}^{\text{ff}}(\vec{r}) = \frac{1}{2\eta} \left| \vec{E}_{J,K,\text{total}}^{\text{ff}}(\vec{r}) \right|^2 \hat{r} \quad (6)$$

Similarly, the total power radiated (the total flux of the Poynting vector through the sphere at infinity  $S_{\infty}^2$ ) is

$$P_{\text{total}}^{\text{rad}} = \iint_{S_{\infty}^2} d\Omega \left[ \hat{r} \cdot \vec{S}_{\omega,\text{total}}^{\text{ff}}(\vec{r}) \right] \quad (7)$$

where  $d\Omega = r^2 \sin\theta d\theta d\phi$ . Finally, the total directivity is

$$D_{\text{total}}(\theta, \phi) = \lim_{r \rightarrow \infty} \frac{4\pi r^2 \left[ \hat{r} \cdot \vec{S}_{\omega,\text{total}}^{\text{ff}}(\vec{r}) \right]}{P_{\text{total}}^{\text{rad}}} \quad (8)$$

The MDM in Fig. 1(b) consists of four electric dipoles and one magnetic dipole. Two electric dipoles are on the y-axis and two are parallel to the y-axis at the height  $d_1$  along the z-axis. One pair of these upper and lower dipoles is displaced from the origin along the -y-axis at a distance  $d_2/2$ ; they have the opposite orientation, the top one being pointed in the +y-direction. The other pair is displaced from the origin along the +y-axis at a distance  $d_2/2$  and has the same orientations. The magnetic dipole element is oriented along the -x-axis and is at the height  $d_3$  along the +z-axis. As shown in Fig. 1(b), their current amplitudes are: bottom two electric dipoles  $i_{e1}$ ,  $i_{e1}'$ ; top two electric dipoles  $i_{e2}$ ,  $i_{e2}'$ ; and the magnetic dipole  $i_{m1}$ . Consequently, the far-field electric field expressions are

$$\vec{E}_{\omega,J}^{\text{ff}}(\vec{r}) = +j\omega\mu G(r) A F_e(r, \theta, \phi) [\hat{r} \times \hat{r} \times \hat{y}] \quad (9)$$

$$\vec{E}_{\omega,K}^{\text{ff}}(\vec{r}) = +j\omega\mu \frac{G(r)}{\eta} A F_m(r, \theta, \phi) [\hat{r} \times (-\hat{x})]$$



where the array factors of the electric and magnetic dipoles are:

$$\begin{aligned}
 AF_e(r, \theta, \phi) &= \sum_{n=1}^4 I_{en} l_{en} e^{+jk\hat{r} \cdot \vec{r}_{en}} \\
 &= -I_{e1} l_{e1} e^{+j(kd_2/2) \sin \theta \sin \phi} \\
 &\quad -I_{e1'} l_{e1'} e^{-j(kd_2/2) \sin \theta \sin \phi} \\
 &\quad +I_{e2} l_{e2} e^{+j(kd_2/2) \sin \theta \sin \phi + j(kd_1) \cos \theta} \\
 &\quad +I_{e2'} l_{e2'} e^{-j(kd_2/2) \sin \theta \sin \phi + j(kd_1) \cos \theta}
 \end{aligned} \tag{10}$$

$$AF_m(r, \theta, \phi) = +I_{m1} l_{m1} e^{+j(kd_3) \cos \theta}$$

The associated vector fields follow immediately with the expressions:

$$\begin{aligned}
 \hat{r} \times \hat{r} \times \hat{y} &= -\cos \theta \sin \phi \hat{\theta} - \cos \phi \hat{\phi} \\
 \hat{r} \times \hat{x} &= \sin \phi \hat{\theta} + \cos \theta \cos \phi \hat{\phi}
 \end{aligned} \tag{11}$$

The electric and magnetic dipole fields thus take the forms:

$$\begin{aligned}
 \vec{E}_{\omega, J}^{\text{ff}}(\vec{r}) &= -j\omega\mu G(r) AF_e(r, \theta, \phi) \\
 &\quad \times [\cos \theta \sin \phi \hat{\theta} + \cos \phi \hat{\phi}]
 \end{aligned} \tag{12}$$

$$\begin{aligned}
 \vec{E}_{\omega, K}^{\text{ff}}(\vec{r}) &= -j\omega\mu \frac{G(r)}{\eta} I_{m1} l_{m1} e^{+j(kd_3) \cos \theta} \\
 &\quad \times [\sin \phi \hat{\theta} + \cos \theta \cos \phi \hat{\phi}]
 \end{aligned}$$

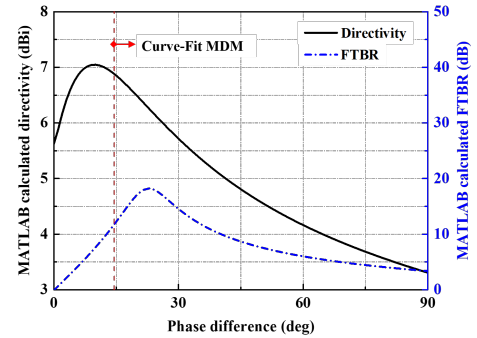
A MATLAB program based on Eqs. (10) and (12) was implemented to calculate the directivity patterns of the multiple dipole-based models.

The MDM's distances were set to those of the prototype:  $d_1 = 0.06 \lambda_{\text{res}}$ ,  $d_2 = 0.15 \lambda_{\text{res}}$ , and  $d_3 = 0.03 \lambda_{\text{res}}$ . The dipole amplitude terms of the MDM were set to:  $I_{e1} l_{e1} = I_{e1'} l_{e1'}$  and  $I_{e2} l_{e2} = I_{e2'} l_{e2'}$ ; its phases were set to:  $\varphi_{e2} = \varphi_{e2'}$  and  $\varphi_{e1} = \varphi_{e1'} = \varphi_{m1} = 0$ . The phase difference is  $\varphi = \varphi_{e2} - \varphi_{e1}$ . The ratio of the current moments  $I_{e1} l_{e1}$  and  $I_{e2} l_{e2}$  and the phase difference  $\varphi$  (i.e., the phase  $\varphi_{e2}$ ) were varied and the radiated field performance was calculated. The directivity patterns were compared with those obtained from the HFSS simulations. Matching those patterns in the forward direction as close as possible, the following relative CMM values:  $I_{e1} l_{e1} : I_{e1'} l_{e1'} : I_{e2} l_{e2} : I_{e2'} l_{e2'} = 1.0 : 1.0 : 0.92 : 0.92$ , and the phase difference  $\varphi = 14.6^\circ$  were obtained. With these curve-fit values, the MDM peak directivity and FTBR values predicted with Eqs. (10) and (12) were 6.78 dBi and 12.37 dB, respectively. As demonstrated in Table III, these final values are quite close to the HFSS calculated ones, 6.75 dBi and 12.18 dB, respectively.

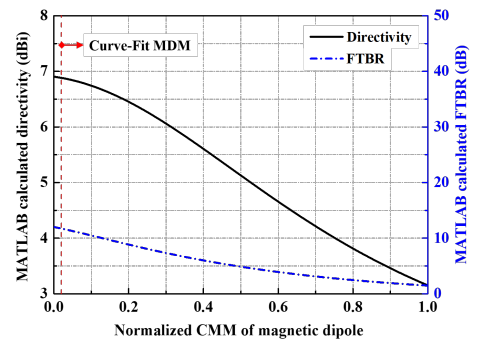
To further illustrate the outcomes of the parameter study, the MDM MATLAB calculated peak directivity and FTBR values when the curve-fit CMM magnitudes remained the same but the phase difference was varied, are presented in Fig. 9(a). On the other hand, with the same CMMs of the electric dipoles and the phase difference fixed at  $\varphi = 14.6^\circ$ , the CMM of the magnetic dipole was varied. Those peak directivity and FTBR values are given in Fig. 9(b). The curve-fit results in both

cases are indicated by the vertical dotted lines. These results clearly illustrate that there is a tradeoff between a high peak directivity and the FTBR value.

The E-plane and H-plane directivity patterns for several of the Fig. 9(b) cases are presented in Fig. 10. They indicate that the magnetic dipole with a small current moment magnitude, e.g., with its normalized value being less than 0.1, has little impact on the broadside radiation performance. On the other hand, it has a definite impact on the beamwidth of the back lobe.



(a)



(b)

Fig. 9. Parameter study of the directivity and FTBR values of the MDM of the ESDA in Section III as functions of the (a) phase difference, and (b) normalized CMM of the magnetic dipole.

## REFERENCES

- [1] A. Goldsmith, *Wireless Communications*. Cambridge, U.K.: Cambridge Univ. Press, 2005.
- [2] J. J. Yu and S. Lim, "Design of multi-band, compact parasitic array with twisted, helical directors," *IEEE Trans. Antennas Propag.*, vol. 61, no. 1, pp. 444–449, Jan. 2013.
- [3] Z. Popović, E. A. Falkenstein, D. Costinett, and R. Zane, "Low-power far-field wireless powering for wireless sensors," *Proc. IEEE*, vol. 101, no. 6, pp. 1397–1409, Jun. 2013.
- [4] N. C. Karmakar, Eds., *Handbook of Smart Antennas for RFID Systems*. Piscataway, NJ: John Wiley & Sons, Inc., 2010.
- [5] P. S. Hall and Y. Hao, Eds., *Antennas and Propagation for Body-Centric Wireless Communications*, 2nd ed. Norwood, MA: Artech house, 2012.
- [6] M. Pigeon, C. Delaveaud, L. Rudant, and K. Belmkaddem, "Miniature directive antennas," *Int. J. Microw. Wireless Technol.*, vol. 6, no. 1, pp. 45–50, Feb. 2014.
- [7] R. P. Haviland, "Supergain antennas: Possibilities and problems," *IEEE Antennas and Propag. Mag.*, vol. 37, no. 4, pp. 13–26, Aug. 1995.

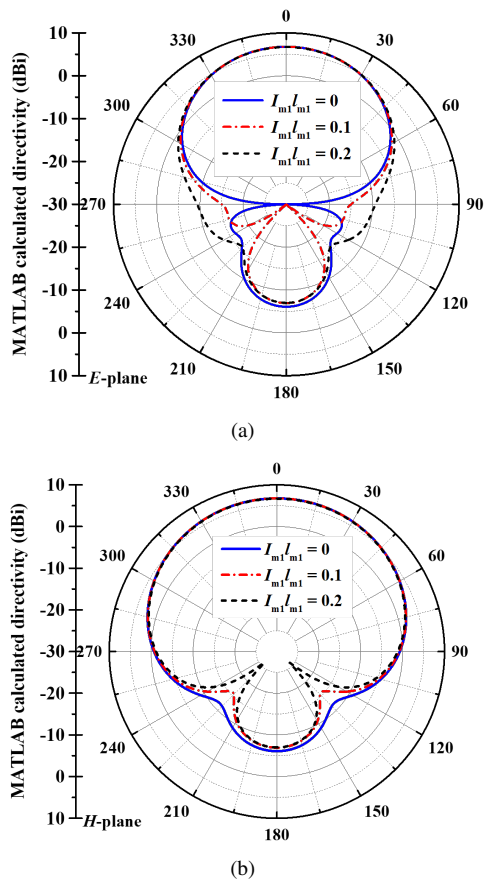


Fig. 10. Parameter study of the MDM of the ESDA in Section III directivity patterns as functions of the normalized CMM of the magnetic dipole. (a) E-plane and (b) H-plane.

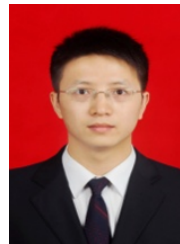
- [8] L. J. Chu, "Physical limitations of omni-directional antennas," *J. Appl. Phys.*, no. 19, Dec. 1948.
- [9] R. F. Harrington, "On the gain and beamwidth of directional antennas," *IEEE Trans. Antennas Propag.*, vol. 6, no. 3, pp. 219–225, Jul. 1958.
- [10] R. C. Hansen, *Microwave Scattering Antennas*. New York: Academic Press, 1966.
- [11] R. C. Hansen, "Fundamental limitations in antennas," *Proc IEEE*, vol. 69, no. 2, pp. 170–182, Feb. 1981.
- [12] P. Kildal and S. R. Best, "Further investigations of fundamental directivity limitations of small antennas with and without ground planes," in *Proc. 2008 IEEE Antennas and Propagation Society International Symposium*, San Diego, CA, 2008, pp. 1–4.
- [13] P. Kildal, E. Martini, and S. Maci, "Degrees of freedom and maximum directivity of antennas: A bound on maximum directivity of nonsuperdirective antennas," *IEEE Antennas and Propag. Mag.*, vol. 59, no. 4, pp. 16–25, Aug. 2017.
- [14] R. W. Ziolkowski, "Huygens multipole arrays to realize unidirectional needle-like radiation," *Phys. Rev. X*, vol. 7, p. 031017, Jul. 2017.
- [15] M. Gustafsson and M. Capek, "Maximum gain, effective area, and directivity," *IEEE Trans. Antennas Propag.*, vol. 67, pp. 5282–5293, Aug. 2019.
- [16] A. I. Uzkov, "An approach to the problem of optimum directive antennae design," *Comptes Rendus (Doklady) de l'Academie des Sciences de l'URSS*, vol. 53, pp. 35–38, 1946.
- [17] P. Hazdra, J. Kracek, and T. Lonsky, "On end-fire super directivity of arrays of two elementary dipoles and isotropic radiators," *IET Microwaves, Antennas & Propag.*, vol. 13, no. 14, pp. 2405–2411, Mar. 2019.
- [18] A. Clemente, M. Pigeon, L. Rudant and C. Delaveaud, "Design of a super directive four-element compact antenna array using spherical wave expansion," *IEEE Trans. Antennas Propag.*, vol. 63, no. 11, pp. 4715–4722, Nov. 2015.
- [19] S. Lim and H. Ling, "Design of a closely spaced, folded Yagi antenna," *IEEE Antennas Wireless Propag. Lett.*, vol. 5, pp. 302–305, 2006.
- [20] A. D. Yaghjian, T. H. O'Donnell, E. E. Altshuler, and S. R. Best, "Electrically small supergain end-fire arrays," *Radio Sci.*, vol. 43, no. 03, pp. 1–13, June 2008.
- [21] Z. Bayraktar, P. L. Werner, and D. H. Werner, "The design of miniature three-element stochastic Yagi-Uda arrays using particle swarm optimization," *IEEE Antennas Wireless Propag. Lett.*, vol. 5, pp. 22–26, 2006.
- [22] O. S. Kim, S. Pivnenko, and O. Breinbjerg, "Superdirective magnetic dipole array as a first-order probe for spherical near-field antenna measurements," *IEEE Trans. Antennas Propag.*, vol. 60, no. 10, pp. 4670–4676, Oct. 2012.
- [23] E. E. Altshuler, T. H. O'Donnell, A. D. Yaghjian, and S. R. Best, "A monopole superdirective array," *IEEE Trans. Antennas Propag.*, vol. 53, no. 8, pp. 2653–2661, Aug. 2005.
- [24] T. Kokkinos and A. P. Feresidis, "Electrically small superdirective endfire arrays of metamaterial-inspired low-profile monopoles," *IEEE Antennas Wireless Propag. Lett.*, vol. 11, pp. 568–571, 2012.
- [25] C. A. Balanis, *Antenna Theory: Analysis and Design*. Piscataway, NJ: John Wiley & Sons, 2016.
- [26] R. W. Ziolkowski, P. Jin, and C.-C. Lin, "Metamaterial-inspired engineering of antennas," *Proc. IEEE*, vol. 99, pp. 1720–1731, Oct. 2011.
- [27] Y. Dong and T. Itoh, "Metamaterial-based antennas," *Proc. IEEE*, vol. 100, no. 7, pp. 2271–2285, Jul. 2012.
- [28] R. W. Ziolkowski, "AWE-inspiring electrically small antennas," *Reviews of Electromagnetics (RoE)*, 2021, <https://www.euraap.org/papers>, <https://en.calameo.com/read/006775127fac88ee6689>.
- [29] D. F. Sievenpiper, D. C. Dawson, M. M. Jacob et al., "Experimental validation of performance limits and design guidelines for small antennas," *IEEE Trans. Antennas Propag.*, vol. 60, no. 1, pp. 8–19, Jan. 2012.
- [30] A. Erentok, P. L. Luljak, and R. W. Ziolkowski, "Characterization of a volumetric metamaterial realization of an artificial magnetic conductor for antenna applications," *IEEE Trans. Antennas Propag.*, vol. 53, no. 1, pp. 160–172, Jan. 2005.
- [31] F. Yang and Y. Rahmat-Samii, *Electromagnetic Band Gap Structures in Antenna Engineering*. Cambridge, UK: Cambridge University Press, 2009.
- [32] P. Jin and R. W. Ziolkowski, "High directivity, electrically small, low-profile, near-field resonant parasitic antennas," *IEEE Antennas Wireless Propag. Lett.*, vol. 11, pp. 305–309, 2012.
- [33] M.-C. Tang and R. W. Ziolkowski, "Efficient, high directivity, large front-to-back-ratio, electrically small, near-field-resonant-parasitic antenna," *IEEE Access*, vol. 1, no. 1, pp. 16–28, May 2013.
- [34] P. Jin and R. W. Ziolkowski, "Metamaterial-inspired, electrically small Huygens sources," *IEEE Antennas Wireless Propag. Lett.*, vol. 9, pp. 501–505, 2010.
- [35] M.-C. Tang, B. Zhou, and R. W. Ziolkowski, "Low-profile, electrically small, Huygens source antenna with pattern-reconfigurability that covers the entire azimuthal plane," *IEEE Trans. Antennas Propag.*, vol. 65, no. 3, pp. 1063–1072, Mar. 2017.
- [36] Z. Wu, M.-C. Tang, M. Li, and R. W. Ziolkowski, "Ultralow-profile, pattern-reconfigurable metamaterial-inspired Huygens dipole antenna," *IEEE Trans. Antennas Propag.*, vol. 68, no. 3, pp. 1238–1248, Mar. 2020.
- [37] M.-C. Tang, H. Wang, and R. W. Ziolkowski, "Design and testing of simple, electrically small, low-profile, Huygens source antennas with broadside radiation performance," *IEEE Trans. Antennas Propag.*, vol. 64, no. 11, pp. 4607–4617, Nov. 2016.
- [38] M.-C. Tang, T. Shi, and R. W. Ziolkowski, "A study of 28 GHz, planar, multi-layered, electrically small, broadside radiating, Huygens source antennas," *IEEE Trans. Antennas Propag.*, vol. 65, no. 12, pp. 6345–6354, Dec. 2017.
- [39] W. Lin and R. W. Ziolkowski, "Electrically-small, low-profile, Huygens circularly polarized antenna," *IEEE Trans. Antennas Propag.*, vol. 66, no. 2, pp. 636–643, Feb. 2018.
- [40] M.-C. Tang, Z. Wu, T. Shi, and R. W. Ziolkowski, "Dual-band, linearly polarized, electrically small Huygens dipole antennas," *IEEE Trans. Antennas Propag.*, vol. 67, no. 1, pp. 37–47, Jan. 2019.
- [41] J. J. Yu and S. Lim, "Design of an electrically small, circularly polarized, parasitic array antenna for an active 433.92-MHz RFID handheld reader," *IEEE Trans. Antennas Propag.*, vol. 60, no. 5, pp. 2549–2554, May 2012.
- [42] M.-C. Tang, Q. Lin, M. Li, and R. W. Ziolkowski, "Polarization-reconfigurable Yagi-configured electrically small antenna," *IEEE Trans. Antennas Propag.*, vol. 69, no. 3, pp. 1757–1762, Mar. 2021.
- [43] S. Lim, J. Chen, and C. Cato, "Design of a thin, electrically small, two-element parasitic array with circular polarization," *IEEE Antennas Wireless Propag. Lett.*, vol. 17, no. 6, pp. 1006–1009, Jun. 2018.

- [44] M.-C. Tang, B. Zhou, and R. W. Ziolkowski, "Flexible uniplanar electrically small directive antenna empowered by a modified CPW feed," *IEEE Antennas Wireless Propag. Lett.*, vol. 15, pp. 914–917, 2016.
- [45] A. D. Yaghjian, "Increasing the supergain of electrically small antennas using metamaterials," in *Proc. 2009 3rd European Conference on Antennas and Propagation (EuCAP 2009)*, Berlin, Germany, 2009, pp. 858–860.
- [46] ANSYS Electromagnetics Suite (HFSS) ver. 19 [Online]. Available: <https://www.ansys.com/products/electronics/ansys-hfss> (2018).
- [47] MATLAB, *Matrix Laboratory (MATLAB)*, ver. R2020a, MathWorks Inc. [Online]. Available: <https://www.MATLAB.com> (2020).
- [48] R. W. Ziolkowski, "Mixtures of multipoles – Should they be in your EM toolbox?," *IEEE Open J. Antennas Propag.*, vol. 3, pp. 154–188, 2022.
- [49] R. Rodriguez-Cano and R. W. Ziolkowski, "Single-layered, unidirectional, broadside-radiating planar quadrupole antenna for 5G IoT applications," *IEEE Trans. Antennas Propag.*, vol. 69, no. 9, pp. 5524–5533, Sep. 2021.
- [50] A. C. Durgun, C. A. Balanis, C. R. Birtcher, and D. R. Allee, "Design, simulation, fabrication and testing of flexible bow-tie antennas," *IEEE Trans. Antennas Propag.*, vol. 59, no. 12, pp. 4425–4435, Dec. 2011.
- [51] A. K. Sarychev and G. Tartakovskiy, "Magnetic plasmonic metamaterials in actively pumped host medium and plasmonic nanolasers," *Phys. Rev. B*, vol. 75, 085436, 2007.
- [52] S. Mühlig, C. Menzel, C. Rockstuhl, and F. Lederer, "Multipole analysis of meta-atoms," *Metamaterials*, vol. 5, no. 2-3, pp. 64–73, 2011.
- [53] N.-W. Liu, L. Zhu, Z.-X. Liu, G. Fu, and Y. Liu, "Design approach of a single circularly polarized patch antenna with enhanced AR-bandwidth under triple-mode resonance," *IEEE Trans. Antennas Propag.*, vol. 68, no. 8, pp. 5827–5834, Aug. 2020.
- [54] Y. Dong, Z. Wang, Y. Pan, and J. H. Choi, "Characterization of shorted dipole antennas for low-cost RFID reader applications," *IEEE Trans. Antennas Propag.*, vol. 68, no. 11, pp. 7297–7308, Nov. 2020.
- [55] Z. Hu, Z. Shen, W. Wu, and J. Lu, "Low-profile top-hat monopole Yagi antenna for end-fire radiation," *IEEE Trans. Antennas Propag.*, vol. 63, no. 7, pp. 2851–2857, Jul. 2015.
- [56] V. Iyer, S. N. Makarov, D. D. Harty, F. Nekoogar, and R. Ludwig, "A lumped circuit for wideband impedance matching of a non-resonant, short dipole or monopole antenna," *IEEE Trans. Antennas Propag.*, vol. 58, no. 1, pp. 18–26, Jan. 2010.
- [57] C. Icheln, J. Krogerus, and P. Vainikainen, "Use of balun chokes in small-antenna radiation measurements," *IEEE Trans. Antennas Propag.*, vol. 53, no. 2, pp. 498–506, Apr. 2004.



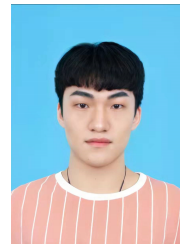
**Ting Shi** (Member, IEEE) received the B.S. degree in electronic information science and technology from University of Electronic Science and Technology of China (UESTC), Chengdu, China, in 2014, and the M.S. and Ph.D. degree in circuit and system from Chongqing University, Chongqing, China, in 2017 and 2020, respectively. In Sep. 2018–Sep. 2019, she was also with the Department of Electrical and Computer Engineering, National University of Singapore (NUS), Singapore, as a Visiting Graduate.

She is currently a Post-Doctoral Fellow in the School of Electronic Science and Engineering (National Exemplary School of Microelectronics), UESTC, Chengdu, China. Her research interests include microwave antenna and array and metasurfaces absorber. Dr. Shi was a recipient of the Student Paper Award in the IEEE 7th Asia-Pacific Conference on Antennas and Propagation (2017 APCAP) and the Newcomer Award for Graduate Candidates in 2019 the 1st China Meta Materials Conference.



**Ming-Chun Tang** (Senior Member, IEEE) received the B. S. degree in physics from the Neijiang Normal University, Neijiang, China, in 2005 and the Ph. D. degree in radio physics from the University of Electronic Science and Technology of China (UESTC), in 2013. From August 2011 to August 2012, he was also with the Department of Electrical and Computer Engineering, The University of Arizona, Tucson, AZ, USA, as a Visiting Scholar. He is currently a full Professor in the School of Microelectronics and Communication Engineering, Chongqing University, China. His research interests include electrically small antennas, RF circuits, metamaterial designs and their applications.

Prof. Tang was a recipient of the National Science Fund for Excellent Young Scholars in 2019. He is the founding Chair of the IEEE AP-S / MTT-S Joint Chongqing Chapter. He has also served on the review boards of various technical journals, and many international conferences as a General Chair, TPC Member, Session Organizer, and the Session Chair.



**Ruolei Chai** (Student Member, IEEE) received the B.S. degree in Kunming University of Science and Technology, Yunnan, China, in 2020. He is currently pursuing the M.S. degree in electronic science and technology with the School of Microelectronics and Communication Engineering with Chongqing University, Chongqing, China.

His current research interests include circularly polarized antennas and metasurface antennas.



**Richard W. Ziolkowski** received the B. Sc. (magna cum laude) degree (Hons.) in physics from Brown University, Providence, RI, USA, in 1974; the M.S. and Ph.D. degrees in physics from the University of Illinois at Urbana-Champaign, Urbana, IL, USA, in 1975 and 1980, respectively; and an Honorary Doctorate degree from the Technical University of Denmark, Kongens Lyngby, Denmark in 2012.

He is currently a Distinguished Professor in the Global Big Data Technologies Centre in the Faculty of Engineering and Information Technologies (FEIT)

at the University of Technology Sydney, Ultimo NSW Australia. He became a Professor Emeritus at the University of Arizona in 2018, where he was a Litton Industries John M. Leonis Distinguished Professor in the Department of Electrical and Computer Engineering in the College of Engineering and was also a Professor in the College of Optical Sciences. He was the Computational Electronics and Electromagnetics Thrust Area Leader with the Engineering Research Division of the Lawrence Livermore National Laboratory before joining The University of Arizona, Tucson, AZ, USA, in 1990. His current research interests include the application of new mathematical and numerical methods to linear and nonlinear problems dealing with the interaction of electromagnetic and acoustic waves with complex linear and nonlinear media, as well as metamaterials, metamaterial-inspired structures, nano-structures, and other classical and quantum applications-specific configurations.

Prof. Ziolkowski was the recipient of the 2019 IEEE Electromagnetics Award (IEEE Technical Field Award). He became a Fellow of Optica (previously the Optical Society of America, OSA) in 2006 and the American Physical Society (APS) in 2016. He was the 2014-2015 Australian DSTO Fulbright Distinguished Chair in Advanced Science and Technology. He served as the President of the IEEE Antennas and Propagation Society (AP-S) in 2005 and has had many other AP-S leadership roles. He is also actively involved with the International Union of Radio Science (URSI), the European Association on Antennas and Propagation (EurAAP), and the International Society for Optics and Photonics (SPIE) professional societies.